

## 1

# One-Dimensional Semiconducting Hybrid Nanostructure: Gas Sensing and Optoelectronic Applications

*Jyoti Rawat, Himani Sharma, and Charu Dwivedi*

*Doon University, School of Physical Sciences, Department of Chemistry, Kedarpuram Dehradun, Uttarakhand, 248001, India*

## 1.1 Introduction

The study and manipulation of matter on the nanoscopic scale is known as nanotechnology. It involves nanoparticles within the size range of 100 nm [1]. The nanomaterial comprises two-dimensional (2D) nanofilms, one-dimensional (1D) nanowires (NWs), and zero-dimensional (0D) nanoparticles [1]. It is widely acknowledged that 1D nanomaterials are quintessential method for investigating a wide range of unique systems at the nanoscale as well as to study the size and dimensional dependency of their functional properties [2]. They are expected to play a key role as both interconnect and fundamental components in nanoscale, optoelectronic, electrochemical, and electromechanical devices. 1D semiconductor nanostructures can be systematically and consistently manufactured in a single-crystalline form with precise control over their chemical composition, diameter, length, and doping level [3, 4]. Nanostructures have made it possible to develop a wide range of prototype devices and integration methodologies [5].

Hybrid nanostructures are made up of at least two unique elements, both of which have as minimum as 1D nanometer scale [6]. Hybrid nanostructures have the ability to combine the benefits of distinct components while overcoming their flaws, resulting in increased efficiency in certain applications or possibly the generation of unique characteristics and/or functions [7]. The shape, crystalline form, exposed facet, spatial organization, component distribution, and interface between components all contribute to the features and functionality of a hybrid nanostructure [8, 9]. As a result, coherent design and controlled manufacturing of hybrid nanostructures are vital for optimizing material performance in specialized applications as well as improving our knowledge of key framework interactions [10].

In general, there are two types of synthetic approaches for constructing 1D nanostructures: top-down and bottom-up. The top-down technique necessitates

horizontal sequencing of bulk materials using either subtractive or additive procedures in order to make nanosized structures [11]. Several technologies, such as gas-phase condensation and wet ball milling, are employed to produce nanostructures utilizing a top-down approach [12]. Although the top-down method has been crucial in the fabrication of nanostructures, it has various disadvantages, including the formation of defects in treated materials, high prices, the necessity for high-surface-finish materials, and longer etching durations. Nanostructures are also built from single atoms or molecules in a bottom-up manner. During the construction of desirable nanostructures (2–10 nm in size range), regulated segregation of atoms or molecules occurs [13]. Some of the technologies used in the bottom-up approach are molecular beam epitaxy (MBE), chemical vapor deposition (CVD), sol-gel technique, laser pyrolysis, metal-organic decomposition, self-assembly processes, and wet synthesis [14].

The application of 1D hybrid nanostructure is also being explored in gas sensing and optoelectronic devices. Regulated development of carbon nanotube (CNT) arrays may be used to fabricate electrical and optoelectronic devices such as field-effect transistors (FETs), photodetectors, and light-emitting diodes (LEDs) for applicability in optoelectronics of 1D nanostructures LED [15, 16]. Y. Zhao et al. explain current advancement on the construction of organic 1D nanostructures and their distinctive optical and electronic properties, along with their use as basic components in optoelectronic functions and devices such as tunable emission, multicolor emission, optical waveguides, lasing, and modulators. The design and manufacturing techniques of structured 1D nanostructures and their possible implementations in optoelectronic devices such as photovoltaic (PV) cells and switches, and the synthesis of 1D organic nanostructures utilizing a range of organic functional materials spanning from polymers to small molecules, are also documented in the literature [17]. Type II antimonide-based superlattices in 1D, for instance, can be employed in infrared photon detectors for implementations in electronics, sensing, biosciences, and plasmonics [18, 19].

This chapter describes 1D hybrid nanostructure such as nanotube, NW, and nanotube and their unique properties. The method of fabrication for such nanostructures is also discussed in brief. Furthermore, this chapter also sheds light on the application of 1D nanostructure in the field of gas sensing and optoelectronic devices.

## 1.2 Synthesis of 1D Hybrid Nanostructures

### 1.2.1 Top-Down Approach

The top-down strategy necessitates horizontal sequencing of bulk materials, using either subtractive or additional processes, to build nanosized morphology [20]. Wet ball milling, gas-phase condensation, and lithography as well as other top-down strategies have been employed by researcher to fabricate nanostructures [21]. The most cost-efficient methods for mass-producing nanomaterials are mechanical techniques. Wet ball milling appears to be the most fundamental of all. Wet ball

milling produces nanomaterials by transmitting kinetic energy from a grinding medium to a material being reduced [21].

Chen et al. employed wet ball milling method to produce hexagonal boron nitride powder which are extremely noncrystalline or amorphous nanoparticles. Boron nitride nanotubes (BNNTs) and nanostructures similar to the bamboo-shaped BN have been developed [22]. When vaporized materials collide with inert gas molecules in the gaseous phase, they dissipate kinetic energy and condense in the form of nanoscopic crystals which can be accumulated on the substrate as an extremely fine powder [23]. Chepkasov et al. reported an experimental investigation of copper nanoparticles condensation from the gas phase, as well as molecular dynamic modeling of a system with 8500 typical copper atoms. The digital model was established to accurately represent the mechanism of vaporization as well as condensation in significant studies. Lithography is a more adaptable and simple approach for generating self-assembled 1D nanostructures on various substrates [24]. Lithography is also a quick and efficient method of surface mapping that is applicable for a large variety of substrates. Lithography refers to a variety of surface processing techniques that include projecting a pattern from a photomask onto a substrate's surface, allowing many duplicates to be created from a single exposure [25]. To complement lithographic techniques for the fabrication of 1D semiconductor nanostructures, several other lithographic techniques such as extreme ultraviolet (EUV) and X-ray lithography (XRL) are being developed [25]. XRL has been extensively explored using radiations in the wavelength range of 0.1–10 nm, as this narrow wavelength range was deemed promising for high-resolution applications [26]. Despite this, quality imaging UV lithography with a 13.5 nm wavelength irradiation is insufficient [27]. However, considering EUV sources have restricted power, enhancing the sensitivity of resists while maintaining design integrity and consistency is a crucial problem for addressing high-volume production throughput demands [27].

### 1.2.2 Bottom-Up Approach

Bottom-up approach have proven to be advantageous over the top-down method as they stands to benefit the preparation of self-assembled nanostructures that exhibit distinctive interdisciplinary characteristics which are distinguishable from the characteristics demonstrated by the independent constructing constituent [28]. CVD process, sol-gel method, MBE process, molecular self-assembly (MSA) process, and wet synthesis are some ways utilized in the bottom-up approach. The method which is broadly used in the semiconductor industrial field for the deposition of thin layers in various substances is CVD [29]. The subsection of the surface to more than one unstable precursors is involved in this process. The reactant is decomposed by the precursors, which interact with it to produce the desirable deposition. In this method, volatilized precursors at the beginning are adsorbed on a surface at a high temperature, which subsequently interact with one another or disintegrate to form crystals [29]. MBE is another method of physical evaporation that does not require any chemical reactions. MBE varies from conventional epitaxy systems because it depends on a simple physical evaporation process rather than chemical

**Table 1.1** 1D hybrid nanostructures, types, method of synthesis, analyte gas molecules, and detection limit.

| Methods of syntheses        | 1D nanostructures type   | Analyte gas      | Detection limit | References |
|-----------------------------|--|------------------|-----------------|------------|
| Hydrothermal                | ZnO nanowire   | H <sub>2</sub> S | 5 ppb           | [34]       |
| Electrospinning             | SnO <sub>2</sub> BNNT  | NO <sub>2</sub>  | 250 ppb         | [35]       |
| Electrochemical anodization | TiO <sub>2</sub> nanotube  | Ethanol          | 100 ppm         | [36]       |
| Electrodeposition           | CuO nanowire   | H <sub>2</sub> S | 2.5 ppb         | [37]       |
| Solvothermal                | ZnO nanotube   | NO <sub>2</sub>  | 500 ppm         | [38]       |
| Oxidation                   | Fe <sub>2</sub> O <sub>3</sub> nanowire                          | NH <sub>3</sub>  | 0.95 ppm        | [39]       |
| Hydrothermal                | TiO <sub>2</sub> nanoparticles                                   | Acetone          | 500 ppb         | [40]       |
| Sol-hydrothermal            | Ag-In <sub>2</sub> O <sub>3</sub> nanorod                        | H <sub>2</sub> S | 0.005 ppm       | [41]       |
| Electrospinning             | In <sub>2</sub> O <sub>3</sub> /reduced graphene oxide nanofiber | NH <sub>3</sub>  | 44 ppb          | [42]       |

interactions. The notion of vacuum evaporation is used in this process, in which hot molecules and atomic rays collide directly with a hot substrate under ultrahigh vacuum conditions [30, 31]. The MBE process has the benefit of operating at a lower temperature than vapor-phase epitaxy. The MSA method excels in producing nanoparticles in the 1–100 nm range [32]. Critical characteristics like distinct geometry and precise interactions between the basic units must be taken into account when creating complex nanostructures utilizing the MSA method. MSA is a noncovalent binding process in which atoms and molecules assemble in a stable and distinct nanophase [33]. Several 1D TiO<sub>2</sub> nanostructures (such as nanorods, NWs, nanotubes, and nanobelts) have been produced for optoelectronic and gas sensor applications throughout, which will be briefly reviewed in the next section (Table 1.1) [43]. The sol-gel method entails merging scattered solid nanoparticles (sols with diameters ranging from 1 to 100 nm) in a homogenous liquid medium and aggregating them to form a coherent three-dimensional (3D) structure in the liquid phase with pore dimensions in the sub-micrometer range [44].

### 1.2.2.1 Nanotubes

CNTs were found soon after fullerenes were successfully synthesized in one experiment. CNTs have been a subject of investigation since their discovery in 1991, owing to their distinctive structural qualities and properties, as well as their potential technological applications [38]. They resemble a cylinder constructed of a graphite sheet (hexagonal carbon lattice). Nanotubes exhibit a variety of electrical, structural, and thermal properties that vary depending on length, diameter, and chirality or twist of the nanotube [45]. To further the interest, nanotubes can have multiple walls (MWNTs) cylinders inside cylinders in addition to a single cylindrical wall (SWNTs) [46]. Sen et al. pyrolyzed adequate components to create boron carbide nitride (B-C-N) and C-N nanotubes. When aza-aromatics, like pyridine, are

pyrolyzed over cobalt catalysts, CN nanotubes are produced. Thermal decomposition of the 1 : 1 addition compound of  $\text{BH}_3$  with  $(\text{CH}_3)_3\text{N}$  yields B–C–N nanotubes.  $\text{C}_{33}\text{N}$  is believed to be the usual composition of C–N nanotubes [46]. Unusual structural morphologies, such as bamboo or nested-cone-shaped cross sections, and others with unique morphologies, such as coiled nanotubes, are commonly observed in doped nanotubes. The B–C–N nanotubes composition changes depending on their mode of synthesis. Moreover, single-walled nanotubes (SWNTs) are the most common product in terms of diameter [47, 48].

### 1.2.2.2 Nanowires

Over the last years, a broad range of physicochemical methods have been reported the fabrication of semiconducting NWs [49]. These strategies might be classified using both bottoms-up and top-down approaches [50]. To create NWs, the physical process relies on cutting bulk single-crystalline materials (such as Si, Ge, and GaAs) with high-energy plasma species [51, 52]. Since Wagner and associates created Au-catalyzed Si micro-whiskers in 1964, the catalyst particle aided vapor–liquid–solid (VLS) growth process, first reported by the production of NWs from diverse materials utilizing a range of physical sputtering, e-beam, MBE, and CVD methods, has been intensively studied [53]. By using traditional methodologies for the development of the epitaxial structure through this VLS method, a precision alignment system may be obtained throughout NW formation. Inside the regulated fabrication of heavy nanofiller arrays and single-wire devices, the approach VLS epitaxy proves to be advantageous [54]. If ZnO is grown multilayered on a flat crystal framework, it tends to enlarge in dimension and readily generates highly oriented arrangements (Figure 1.1a). For the GaN (Figure 1.1b) and Si/Ge structures, a comparable level of epitaxial regulation may be accomplished [55, 56]. This VLS approach may be used to create NW structures with strict shape control ( $<20\text{ nm}$ ) [57, 58]. Advances in scanning and transmission electron microscopy (TEM) provided essential analytical tools for characterizing these materials in the following decades, paving the way for the fabrication of NWs in the field of advanced materials.

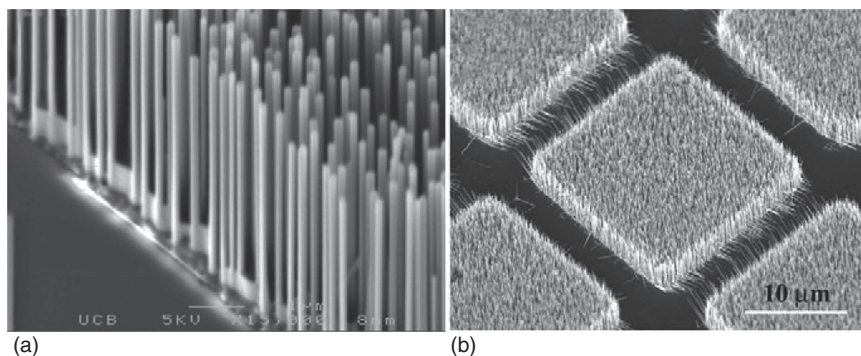


**Figure 1.1** SEM image (a) on a plane sapphire wafer, ZnO nanowires, and (b) GaN nanowire arrays on plane  $\text{LiAlO}_2$  part. Source: Pauzauskie and Yang [56], Elsevier.

### 1.2.2.3 Nanorods

Nanorods are an appealing component for research and often good alternatives for various applications due to their form anisotropy. Due to the increased stimulation of surface plasmons in nanoparticles produced by an increase in particle aspect ratio, nanorods have been shown to be more efficient than spherical particles. The strength of the dipole moment is notably significant within a nanoparticle due to the rise in surface plasmons [59]. As a result, the electrical field in nanorods increases in comparison with spherical particles. Significantly well-oriented CdSe nanorods, according to Alivisatos and coworker, provided an effective, guided path for charge transporters to pass through the photoelectric device and be collected [60]. Inserting nanorods into P3HT films boosted extrinsic quantum yield by three times when the aspect ratio was raised from 1 to 10 nm [61]. While researching Ag nanorods for polystyrene composites by Winey et al., they discovered that the electrical conductivity of polymer composites is influenced by the aspect ratio of anisotropic nanoparticles. Particularly, because rod-shaped particles have a lower percolation threshold than spherical particles [62], percolation threshold was discovered to be affected by both the form and size of nanoparticles. Many advantages in the underlying features of nanorods are projected to be shared by larger rod-shaped particles, both in diameter and length. In conclusion, the aspect ratio, polydispersity, volume fraction, and alignment of nanorods have a significant impact on their efficacy [62].

In general, the development of nanorods in arrays requires a platform supplied by the substrate, which can be constructed of a variety of materials [63]. According to Oh et al., electrochemical gas sensors based on vertically oriented ZnO nanorod arrays (average length and diameter were 500 and 50 ppm, respectively) were successfully created (Figure 1.2a,b) [64, 65]. The devices can be made by introducing 39.5 W/cm ultrasound vibrations at 20 kHz into a solvent (such as 0.1 M zinc nitrate

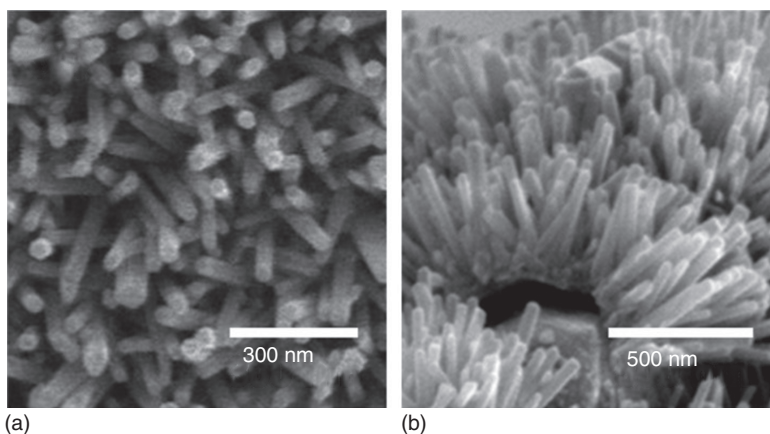


**Figure 1.2** SEM picture of ZnO nanorod (a) upper view and (b) oblique view. Source: Yuan et al. [64], MDPI, CC BY 4.0.

hexahydrate and 0.1 M hexamethylenetetramine) so that the organic material is submerged in the  $\text{Al}_2\text{O}_3$  substratum, where the Pt conductor is stored, and Zn thin films are formed immediately [65].

## 1.3 Applications of 1D Hybrid Nanostructures

### 1.3.1 Gas Sensing

The need for the detection of the small extent of explosive, combustible, and poisonous gases and screening of environmental contamination has given way to the development of various gas sensors [66]. Medicine, agriculture, industrial refining, and environmental studies are the fields that have found the great application of these sensors. Among such highly flammable gases, sensing of lightest element hydrogen is one such case of implementation of gas sensors. It is undetectable by the human eye. Hydrogen on reaction with oxygen results in an inflammable compound that can be ignited with a flame or a spark. The fuel- for hydrogen-powered vehicles and aeronautical operations are being provided by hydrogen [67]. Hydrogen screening is useful for a variety of reasons, from pollution detection to early warning indications of fires or nuclear reactor safety to presenting proof of certain diseases. Detecting the presence and quantity of hydrogen is useful in the manufacturing of semiconductors and the identification of imminent transformer failure in electric power plants. Other examples include volatile organic compounds (VOCs), which as the name suggests have a high vapor pressure [68]. VOCs are plentiful and omnipresent, with some posing a health risk to humans and others being damage to the environment. Hazardous VOCs are not usually dangerous, but if they are created within homes, they might cause sick building syndrome. VOCs can be found in human bodies, and on the other hand, some of the VOCs have intensified long-term health consequences and some are even proven carcinogens [69]. A good sensor should have a high susceptibility, quick response, and good selectivity. The development of low-cost and reliable gas sensors that can function at room temperature continues to be a significant scientific and technological obstacle. The detection methodology of the gas sensors can serve as a basis for the classification of various sensing materials and methods. Alterations in electric characteristics, visual, chromatographic, and calorimetric gas sensing are various methods of detection. When gas interacts with the surface of semiconductor gas sensor (metal chalcogenides, CNTs, and conducting polymer), it alters the main physical properties such as the electrical conductivity and work function of the sensing material [66]. Yang and coworkers used thermal oxidation in an oxygen atmosphere within a horizontal tube furnace to manufacture oriented ZnO nanobelt configurations natively on Zn substrates. The coverage of the ZnO nanobelt array on the substrate seems to be reasonably homogenous, with an aerial density of around  $1014 \text{ nanobelts/m}^2$  [70]. These nanobelts have a root diameter of 100–300 nm, a length of 10–20 mm, and a thickness of 3–4 nm. ZnO nanobelt balls grow directly from Zn microparticles to

generate a thick sheet, with the nanobelts precisely aligned on the microparticle surface, when a layer of micrometer-sized Zn particles is used as the growth medium instead of Zn foil. The ammonia gas sensor made from such as-grown ZnO nanobelt ball arrangements on Si substrates has a high sensitivity and quick responsiveness at room temperature [70, 71].

### 1.3.1.1 Safety Monitoring of Exhaust Gases in Automobile

Gas sensors are commonly found in modern automobiles and serve as either a commodity or a critical engine component [72]. Based on the concentrations of atmospheric gases detected in the air intake manifold, it is becoming increasingly common for a vehicle's electronic control unit (ECU) to naturally close and open the outside air flaps [73]. The most monitored gases are those which are combustible [74]. A pair of CO- and NO<sub>2</sub>-sensitive sensors is commonly mounted to determine the air quality. Automobiles must now strictly adhere to rules to maintain adequate air quality index and, therefore, the gas sensors are now a part of their machinery [75]. The decrease in atmospheric contamination and increase in the fuel efficacy must be the aim of the automotive industries, and modern-day gas sensors can help in achieving this goal by offering flexibility in the design and high sensitivity [72].

Electric car fires, chemically dangerous gas leaks and gas pipeline leaks, and explosions have occurred all around the world, and they are nearly typically caused by combustible and explosive gases such as hydrogen, carbon monoxide, hydrogen sulfide, and others [76]. Resistive gas sensors based on 1D nanomaterials have been thoroughly explored for monitoring common gases such as hydrogen, carbon monoxide, and hydrogen sulfide in order to avoid probable explosion and combustions [77]. These gas sensors offer excellent electronic transmission routes, high susceptibility, and chemical and thermal stability [78, 79]. Kumar et al. constructed Nb nanofibers (NFs) and a reversible and selective resistive gas sensor for room-temperature CO gas detection. At room temperature, these sensors demonstrated CO responses of 22% for 2 ppm and 91% for 400 ppm and were more beneficial with fast response/recovery durations [80].

Wang and coworkers used two-step procedures of VLS and atomic layer deposition (ALD) to create 1D SnO<sub>2</sub>/NiO core-shell nanowires (CSNWs) (Figure 1.3a). The SnO<sub>2</sub>/NiO-100 sensor (with 100 ALD cycles) showed a substantial sensitivity of 114–500 ppm hydrogen below 500 °C, that is nearly fourfold more than virgin SnO<sub>2</sub> NWs, and excellent selectivity even in a complex gas environment (ethanol, acetone, hydrogen, and NH<sub>3</sub>) (Figure 1.3b,c). SnO<sub>2</sub>/NiO CSNWs' increased hydrogen-sensing performance was attributed to their high surface-to-volume ratio, the p-n heterojunction that evolved at the p-NiO-shell/n-SnO<sub>2</sub> core interface, and the effective modification of the NiO shell layer [81, 82]. Nikfarjam and coworkers used a unique electrospinning process with secondary electrostatic fields on electrodes with extremely sharp triangular and rectangular edges to create single-aligned pure TiO<sub>2</sub> NFs and gold nanoparticle (GNP)-TiO<sub>2</sub> NFs for gas-sensing devices (Figure 1.3d,e). GNPs-TiO<sub>2</sub> NFs had a lower working temperature (250 °C) than pure TiO<sub>2</sub> NFs and had high susceptibility (70–30 ppb CO) and a lower limit of detection (70 ppt) (Figure 1.3f,g). Through the local Surface Plasmon Resonance (LSPR)

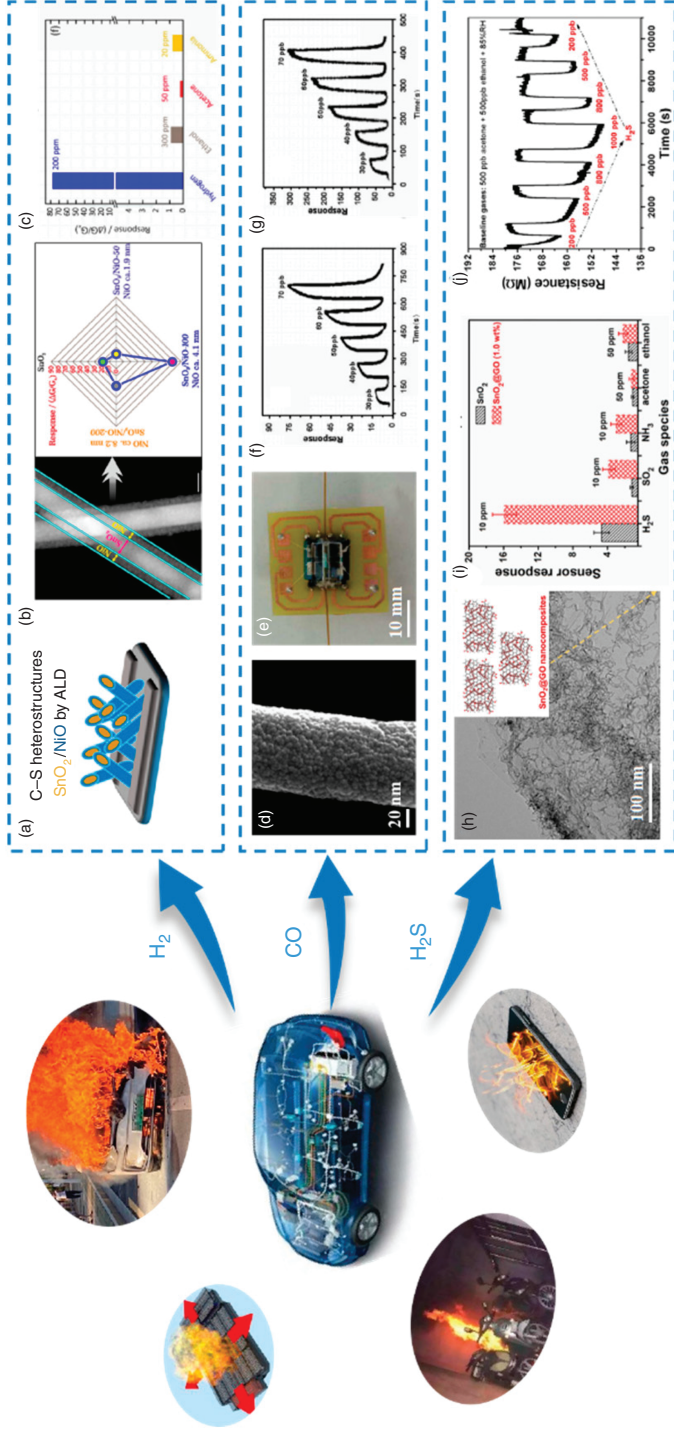


**Figure 1.3** (a) Diagrammatic illustration of SnO<sub>2</sub>/NiO-X CSNWs; (X is the number of atomic layer deposition cycles) (b) SEM image and sensing response of the SnO<sub>2</sub>/NiO-X CSNWs heterostructures toward 200 ppm of H<sub>2</sub> at 50 °C as a function of the NiO-shell layer thickness; (c) at 500 °C, the SnO<sub>2</sub>/NiO-100 sensor response to 200 ppm H<sub>2</sub> and additional interfering gases (300 ppm ethanol, 50 ppm acetone, and 20 ppm NH<sub>3</sub>); (d) TEM image of TiO<sub>2</sub> NFs; (e) picture of the GNP-TiO<sub>2</sub> sensor; time-dependent response; (f) pristine TiO<sub>2</sub> at 300 °C; (g) GNP-TiO<sub>2</sub> at 250 °C in various concentration levels; (h) SEM image of the GNP-TiO<sub>2</sub> sensor; schematic diagram; (i) at 700 °C, the detection performance of the SnO<sub>2</sub>-GO gas sensor and SnO<sub>2</sub>-GO gas sensor to various gases (10 ppm H<sub>2</sub>S, 10 ppm SO<sub>2</sub>, 10 ppm NH<sub>3</sub>, 50 ppm acetone, and 50 ppm ethanol); and (j) the SnO<sub>2</sub>-GO gas sensor (70 °C, RH85%) was used to detect a lower content of H<sub>2</sub>S ranging from 200 to 1000 ppb in acetone (500 ppb) and ethanol (500 ppb) mixture. Source: Wang et al. [81]/MDPI/Public Domain CC BY 4.0.

phenomenon, visible light can activate GNPs, decreasing the reaction's activation energy in the process. It is observed that, when GNPs came into proximity of TiO<sub>2</sub> nanograins, a Schottky barrier formed between them, and electrons passing from the TiO<sub>2</sub> nanograins to the GNPs enlarged the TiO<sub>2</sub> nanograins' depletion zone, reducing sensor conductivity. H<sub>2</sub>S is also one of the combustible and dangerous gases that, when subjected to heat or introduced to open flames, it can form an explosive mixture with air, resulting in combustion. More interestingly, it showed a ppb-level H<sub>2</sub>S reaction in a gas combination containing H<sub>2</sub>S, acetone, and ethanol, with 85% humidity (Figure 1.3j). Pure SnO<sub>2</sub> quantum wires and the GO nanosheet cooperated together to increase transducer performance and chemical reception, resulting in high responsiveness and specific gas sensing. Due to its room-temperature fabrication, low-temperature operation, and great compatibility with the paper substrate, the SnO<sub>2</sub>-GO sensor is a potential adaptable gas sensor. Song et al. used a simple mechanical stirring approach to make SnO<sub>2</sub> quantum wire/GO nanosheets (Figure 1.3h). At low temperatures, the SnO<sub>2</sub>-GO sensor outperformed a pure SnO<sub>2</sub> sensor in terms of responsiveness and specificity to H<sub>2</sub>S (Figure 1.3i) [83].

### 1.3.1.2 Health Monitoring

Gas sensors which are made up of semiconductors are used in practically every industry and have a wide range of applications. Underground miners are vulnerable to combustible gas, asphyxiates, lower oxygen levels, and other poisonous gases [84]. Anchored and transportable sensors are utilized to ensure that in the event of an emergency gas leak, audiovisual alerts are activated, allowing for a safe and quick evacuation of the manpower [85]. Similarly, many different gas detectors are used in the gas and oil industries because of the existence of dangerous random moving molecules, whether during production, transportation, processing, storage, or near distribution pipes [86]. Chemical facilities in almost every sector around the globe are responsible for the release of dangerous gases as by-products during their processes which includes benzene, ethylene, propylene, and toluene produced by the petrochemical sector, H<sub>2</sub>S, and SO<sub>2</sub> produced by the drilling and extraction industries, exposing people living near companies to harmful gases [87]. That makes the availability of highly efficient gas-sensing systems in such sectors imperative.

In the food industry, smart food packaging involves a variety of gas sensors to determine the optimal food/meat aging time, monitor the quality of meat, and control food quality in general [87]. The clever packaging approach allows us to monitor the state of edibles as well as the package's surroundings [88]. As a result, using gas sensors in the food manufacturing and packing industries might dramatically minimize food waste while also lowering the annual number of food poisonings, therefore, enhancing food safety [89]. However, a few of the chemicals found in the body may be used for medical diagnostics, and detection of these unique gases has been proved to be useful in the diagnostic industry. Toluene (lung cancer), isoprene (heart disease), formaldehyde (lung cancer), and NH<sub>3</sub> (hemodialysis) are few examples of such type of chemicals [89]. Ama et al. used nanocomposites including 1D KWO (K<sub>2</sub>W<sub>7</sub>O<sub>22</sub>) nanorods and 2D Ti<sub>3</sub>C<sub>2</sub>T<sub>x</sub> nanosheets to construct a novel acetone

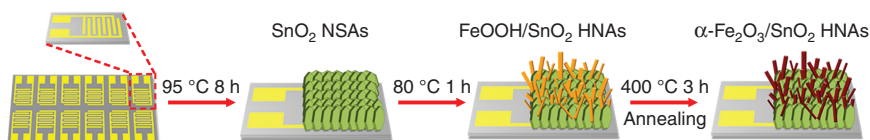


**Figure 1.4** The advancement of  $\text{Fe}_2\text{O}_3/\text{SnO}_2$  reaction. Source: [92] Research A Science Partner Journal / Public Domain CC BY 4.0.

sensor. These nanocomposites have a high acetone sensitivity (10 times that of a KWO-based sensor), a considerable higher atmospheric condition tolerance, and months of increased stability, showing its promising application as a highly accurate as well as precise methanol detecting element in medical care and insulin treatment [90]. Wang et al. developed a poly(styrene-butadiene-styrene)/carbon nanotubes (SBS/CNT) hybrid fiber detector that used a modular wet spinning method to increase selectivity (19–10% solvent) across the entire sensing distance of 100–400 ppm, as well as a quick response (40 seconds) or brilliant mechanical dependability. This sensor showed a lot of potential for health monitoring in wearable and flexible electronic devices [91]. In an easy two-stage CVD process, Gong et al. created a biosensor for alcohol depending on  $\alpha\text{-Fe}_2\text{O}_3/\text{SnO}_2$  heterogeneous structure. There was an increase in sensitivity with outstanding alcohol characteristics in systems based on solid  $\text{SnO}_2$  nanosheets or  $\text{Fe}_2\text{O}_3$  nanorods. A heterojunction using 1D/2D hybridization designs ( $\text{Fe}_2\text{O}_3$ ) could explain the higher productivity ( $\text{SnO}_2$ ). Furthermore, the  $\text{Fe}_2\text{O}_3/\text{SnO}_2$  had remarkable reproducibility, indicating these materials might be used in exhalation testing (Figure 1.4) [92].

### 1.3.1.3 Environmental Monitoring

Poor air quality index in the urban areas are posing a threat to the health of the living beings in such areas. Many respiratory disorders and environmental issues can be tracked down to the emission of harmful gases from chemical power plants and petroleum and mining industries [93]. Natural, synthetic, and anthropogenetic gases are the three types of gaseous contaminants [94]. Natural causes of air pollution include volcano eruptions, wildfires, and lightning, whereas synthetic sources include emissions from human activities such as automobile exhaust gases, chemical disasters, or commercial activity, for example transformers and land disposal [95]. As a direct consequence of climate change due to the increase in the greenhouse gases, the need for monitoring such pollutants is more than ever [95]. The predominant objective of air pollution control is improvement in the air quality index and, therefore, reduced respiratory illness [96]. This includes a screening of gases like  $\text{CO}_2$ ,  $\text{NO}_2$ ,  $\text{SO}_2$ , and  $\text{O}_3$  through befitting gas sensors [89]. Suh et al. developed an edge-exposed  $\text{WS}_2$  manufactured on  $\text{SiO}_2$  NRs that can detect  $\text{NO}_2$  extremely accurately as well as precisely. It reacted to 5 ppm  $\text{NO}_2$  with a response that was significantly greater than the reaction to interfering gases at ambient temperature (3.44 ppm to CO and 0.47 ppm to  $\text{H}_2\text{S}$ ) [97]. The excellent performance of  $\text{WS}_2$  is largely due to its very porous 1D nanomaterials as well as highly sensitive interface regions, which serve as beneficial catalyst surfaces for immediate contact with specific atoms [98].

Lim et al. developed Au-SnO<sub>2</sub> NFs that can detect NO<sub>2</sub> gas at low conditions while exposed to photons (Figure 1.5a). The sensor's exceptional transparency (93%) was aided by the incredibly minimal coverage of sensing materials (approximately 0.3%), allowing the substance to be completely open to the gas and, therefore, facilitate thermal detection as well as photosensitivity process (Figure 1.5b). The packed Au particles amplified the reactivity to NO<sub>2</sub> due to the surface plasmon resonance effect of Au. The sensor had increased responsiveness (300) in daylight to 5 ppm NO<sub>2</sub>, consistent response to sub-ppm NO<sub>2</sub>, and a low activation range of 6 ppb with a high NO<sub>2</sub> reaction in all dried or slightly moist atmospheres (50% and 70%, respectively) (Figure 1.5d,e). A gas sensor with high visibility and ambient temperature functionality would assist in improving transparent digital gadgets and optoelectronic devices which are directly connected to the Internet of Things (IoT) (Figure 1.5) [99]. To synthesize silver nanocrystal (NC)-functionalized multiwalled carbon nanotubes (Ag NC-MWCNTs), Cui et al. employed a simple mini-arc plasma technique combined with an electromagnetic pressure assembling method (Figure 1.5f). When Ag NCs were added to MWCNTs, the susceptibility to NH<sub>3</sub> gas was greatly enhanced (Figure 1.5g). The performance of the gas sensor is significantly influenced by the oxidized Ag surface. NH<sub>3</sub> particles bind to Ag hollow areas on the AgO interface when H is directed against Ag. A positive energy exchange from NH<sub>3</sub> to the Ag NC-MWCNTs hybrid results in a conductance change. The sensor also had high selectivity for various gases and was easy to maintain over time (Figure 1.5h,i) [100].

### 1.3.2 Optoelectronic Application

Optoelectronics is among the most intriguing areas of applicability for hybrid nanostructures due to the ocular and electrical attributes of isolated semiconductors and metal nanoparticles [101]. Indeed, hybrid designs hold the possibility of combining greater potentiality, superior performance, and scaling down of optoelectronic devices, hence enhancing the performance of the device, speed, and power efficiency [101, 102]. The expanded features of hybrid nanostructures might have a significant impact on the disciplines of photodetection and PVs in particular. PV systems are often regarded as among the most efficient and essential strategies for meeting the rising world's energy demands [103]. From the many existing approaches, PVs are deemed being the safest technique to accomplish the desired results through solar energy conversion. Because of their capacity to cost-effectively change conventional catalyst PV radiation as a supply of solar energy, small-molecule and polymer-based PVs have attracted much interest in both industry and academia [104]. Nanoscopic proportions and quicker carrier collection owing to short transit routes are some of the restrictions resolved by semiconductor NWs [55]. Decreasing dimensions underneath the typical absorption depth, on the other hand, impede effective light trapping, lowering overall efficacy. Metal nanostructures can be included in optoelectronics as well as PV-nanostructured methods to improve optical absorbance by enhancing electrical charge [104]. For comparison, near-field coupling between plasmonic nanostructures in close proximity to GaAs NWs was

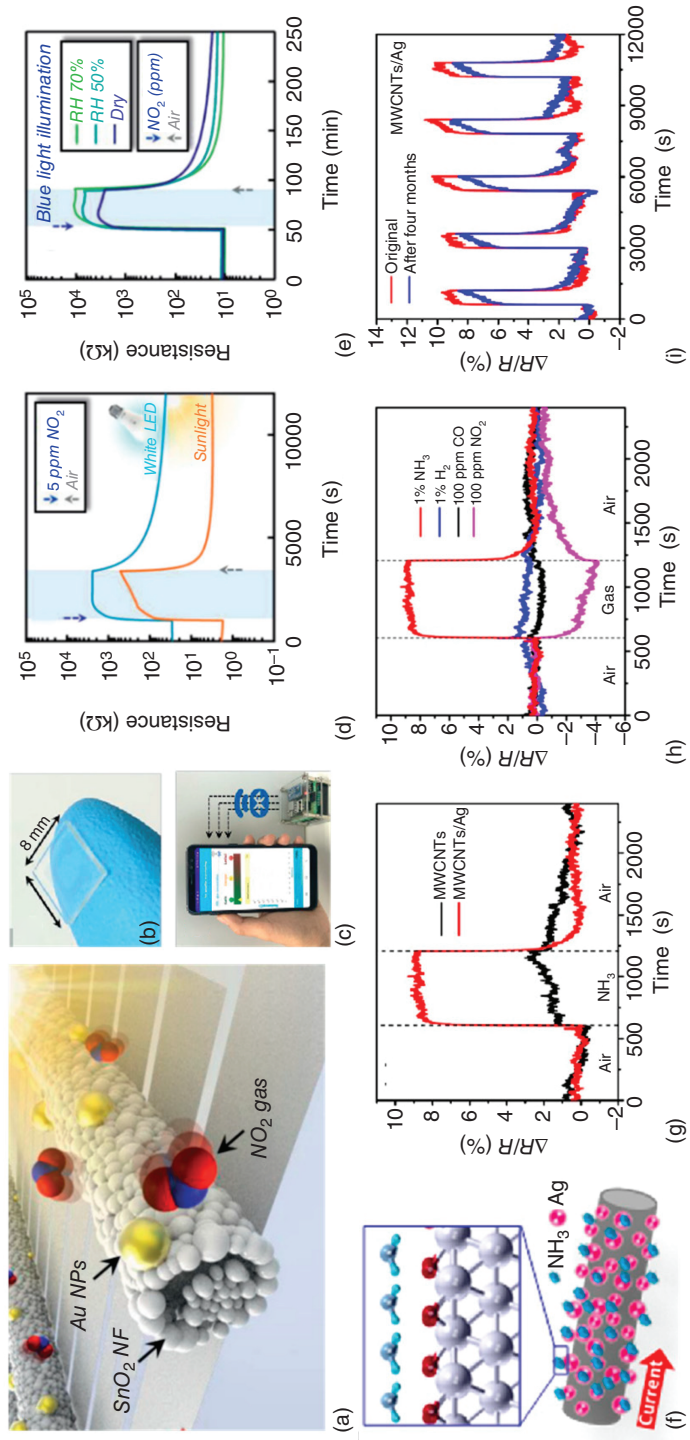


**Figure 1.5** (a) Au-SnO<sub>2</sub> NFs diagrammatic representation; (b) transparency detector images; (c) smart sensor component that can interact with smart phones; (d) resistivity shift in reaction to 5 ppm NO<sub>2</sub> with white LED and sunshine; (e) for various environments; (f) Ag NC MWCNTs graphic demonstration; (g) room-temperature multidimensional sensitivity reaction during Ag NCs decoration; (h) analysis of sensor responses to different chemicals; and (i) characterization of sensing reaction to 1% NH<sub>3</sub> during four months of storage in air. Source: Wang et al. [81], MDPI, CC BY 4.0.

used to reroute electromagnetic waves into the semiconductor and increase intensity up to 20 times for the chosen wavelength and polarization, allowing for the customization of the nonlinear optical response of a single NW [55].

Hyun and coworkers used scanning visible light spectroscopy to correct a localized photocatalytic activity increase of 20% across a Si nanostructure coated with nanocomposite with the horizontal direction. The interaction with the electromagnetic spectra was improved by narrowing the gap between the metallic nanoparticles as well as the Si nanostructure to the semi-region, leading to a twofold increase in photocurrent over the unprotected NWs [105]. Grinblat et al. created ZnO nanostructure by inserting a gold qualitative oligomer within the electric current hot-spots. The author has also reported the interplay between leaky-mode resonances (LMRs) in NWs and limited interface vibrational modes. LMRs are electronic patterns provided by a dielectric cavity in a single silicon-based nanostructure, wherein absorbance is resonance increased. The leaky nature of all these phases aided the interfacial resonances of metallic nanoparticles on the NW substrate. The ensuing coupling allows for the suppression, enhancement, and shifting of absorption resonances, greatly increasing the amount of control over tenability and optical characteristics modulation [106]. Knight et al. investigated the alternative mechanism of hot electron emission through plasmonic degeneration for sensor applications for the first time [107]. Using temperatures beyond the optoelectronic visible region, this indicated system, which was composed of such an arrangement of Au nanostructures constructed atop an n-type Si surface, produced a vibrational frequency and isotropic photon energy with a maximum value of 0.01%. This concept was recently accomplished in near-infrared photodetection devices made of Au nanorods and ZnO NWs. Au nanorod surface plasmons were utilized as reactive ingredients in the suggested idea to create or transmit hot electrons into the huge absorption coefficient ZnO NW, functioning as an inactive material for electronic conductivity. Kawawaki and coworkers enhanced the near-infrared absorbance of PbS QD/ZnO NW PV by integrating Ag nanotubes, improving the electrical properties from 4.5% to 6%. Inside the solid-state p–n power generation system, core–shell silicon NW PVs ornamented with single silver nanomaterials indicated short-wave progression of the short-circuit current (i.e. absorption) emerging both from near-field and far-field coupling with dipolar and quadrupolar nanocrystalline spectra [108]. Weiwei et al. established a solution-phase technique to create a CsPbX<sub>3</sub>/ZnS QDs heterodimer with improved chemical stability and systematic density functional theory-based first-principles calculations backed up this claim. When combined with ZnS, CsPbX<sub>3</sub> exhibits excellent charge dispersion, which is advantageous for PV employments [109].

### 1.3.2.1 Photodetector

Quantum confinement effects can extend bandgaps in nanostructures, and direct bandgaps in semiconductors vary from 1.5 eV (CdTe) to 3.7 eV (ZnS). As a result, nanostructures have a lot of promise for applications such as near infrared (NIR) to UV nanophotodetectors (nano-switches) [55]. Nanostructures are estimated to

have substantially greater efficiency and economics than standard film and bulk devices due to their higher absorption coefficient and chemical stability. Several proof-of-concept composite NW photocatalysts were produced due to the increased optical emission in modified nanomaterials [110, 111]. Luo et al. showed a considerable improvement in photodetection effectiveness of CdSe nanoribbons decorated with Au hollow nanoparticles when compared to bare CdSe nanoribbons and nanoribbons adorned with solid nanoparticles [112]. In addition, Au-decorated CdSe and CdTe NWs, Au-decorated ZnO/ZnCdSeTe CSNWs, Ag-decorated ZnO nanorod array LEDs, and Si NW arrays covered with Au nanomaterial-coated graphene sheets all demonstrated superior plasmon increased light transfer efficiency [112].

Dong and Huang et al. utilized a large bandgap hole transport layer with perovskite photoactive layers to create a highly efficient PV-type photodetector [113]. A photodetector with a ZnSe nanoribbon/Si p–n heterojunction was built by Wang and coworkers to augment the functioning of the ZnSe nanoribbon/Si p–n heterojunction system for which Ag nanoparticles were added (Figure 1.6a–c). The system with Ag nanoparticles had a receptivity and detectivity of 184.8 mA/W and  $9.201 \text{ cm Hz}^{1/2} \text{ W}^{-1}$ , respectively, compared to 117.2 mA/W and  $5.86 \text{ cm Hz}^{1/2} \text{ W}^{-1}$  for the system without silver nanomaterial [114]. The very kinetic hot electrons from regionalized surface plasmon resonance stimulation of metallic plasmonic nanoparticles may swiftly migrate to the surrounding ZnSe nanoribbon with a comparable high energy once the heterojunction is illuminated by light [114]. High-performance photodetectors based on hybrid perovskite PV cells have been disclosed by Dou et al. Under standard circumstances, these PV panels seem to have an electrical performance of around 12% [115].

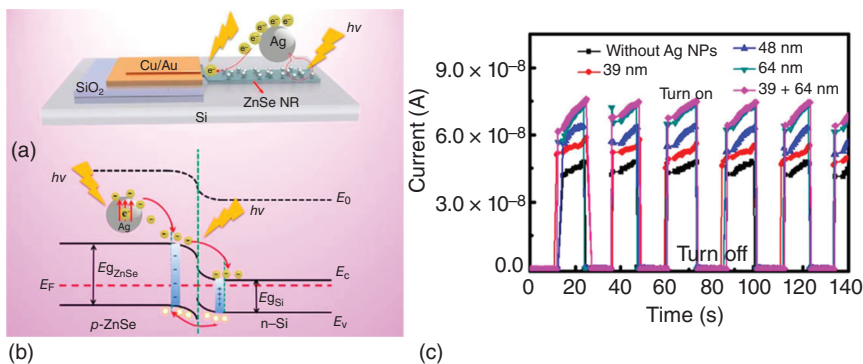


**Figure 1.6** (a) Schematic depiction of localized surface plasmon resonance induced e-transfer from nanomaterials in ZnSe nanoribbon, (b) schematic diagram of the energy bandgap of ZnSe nanoribbon Si heterostructure enhanced with Ag nanomaterial with visible light, and (c) at low voltages, time-domain spectra of the circuit with and without decorating nanomaterials. Source: Zhang [102] / MDPI / Public Domain CC BY 4.0.

### 1.3.2.2 Solar Cell

The bulk semiconductors in the II–VI group have large binding energy and greater light-emitting and transmission coefficients [116]. By integrating semi-material with distinct bandwidth, each section of the heterojunction may preferentially absorb sunlight in a specific spectral region, resulting in more light absorption and better light usage [117]. As a result, heterojunctions have shown great potential in the improvement and advancements of solar cells. CdTe is a viable candidate for solar applications, with a bandgap of 1.45 eV and a greater absorption coefficient [118]. Because a 2 mm CdTe layer absorbs nearly all input direct sunlight, the p-CdTe/n-CdS heterostructures are the least common PV arrangement. Solar cells must be stable to be used in meaningful implementations. Nonetheless, perovskite-based materials, such as CsPbI<sub>3</sub>, which are widely used in PVs, are unsteady and rapidly transition to solar cell that optimized light absorption by rising the interfacial region as well as illumination entrapment. These results mentioned possibilities for solar absorber material selection. TiO<sub>2</sub>–SiO<sub>2</sub> is the cubic perovskite phase in the atmosphere [118]. Wu et al. created solar systems made of CdS, including Ga nanoribbons and Si heterojunctions. During UV activation, the transistors showed PV activity, exhibiting open-circuit photovoltage and short-circuit current of 0.45 V and 3.49 nA, respectively, resulting in a throughput of 44.1% and an energy transfer effectiveness of 1.2% [119].

Zhang and coworkers presented a type II ZnO/ZnSe core–shell nanostructure antireflection materials, which may increase the refractive indices duration via a scattered phenomenon or by producing an optical properties variation in Cu(In, Ga)Se<sub>2</sub> PV [120]. Since using the TiO<sub>2</sub>–SiO<sub>2</sub> core–shell nanostructures to reduce reflectance the efficiency of power conversion increased from 6.32% to 7.00%. CdS/Cu<sub>2</sub>S CSNW solar cells were fabricated by Zhang et al. which had greater open-circuit voltage and fill factor than comparable planar cells and also a 5.4% energy conversion efficiency which is equivalent to their counterpart planar cells when light absorption levels are low. They also used many cells on single nanostructures including both equivalent and consecutive topology to get high emission voltages and currents (Figure 1.7a–f) [102]. A reduced solution-based covalent bond approach, which might also establish a nanocrystalline interface within a single-crystalline CdS core and single-crystalline Cu<sub>2</sub>S shell, is thought to be responsible for the remarkable photocatalytic efficiency of CdS/Cu<sub>2</sub>S core–shell nanostructures [121].

### 1.3.2.3 Light-Emitting Diode

In a perfect PV material, the Shockley–Queisser limit asserts that radioactive decay is the only mechanism for charge recombination [122]. Owing to the recent significant growth in PV efficiency, it has been discovered that hybrid perovskites have extremely high PL quantum yields, which are near 70% at room temperature and nearing 100% at 195 K. This justifies the remarkable PV performance and also actively supports light-emitting device applicability [123]. Huang et al. have made significant change in building electronically driven electroluminescent diode, for example micro-LED, using a variety of semiconductor nanostructures [124]. Despite utilizing nanostructured transistors' growth to create p–n junctions, they employed

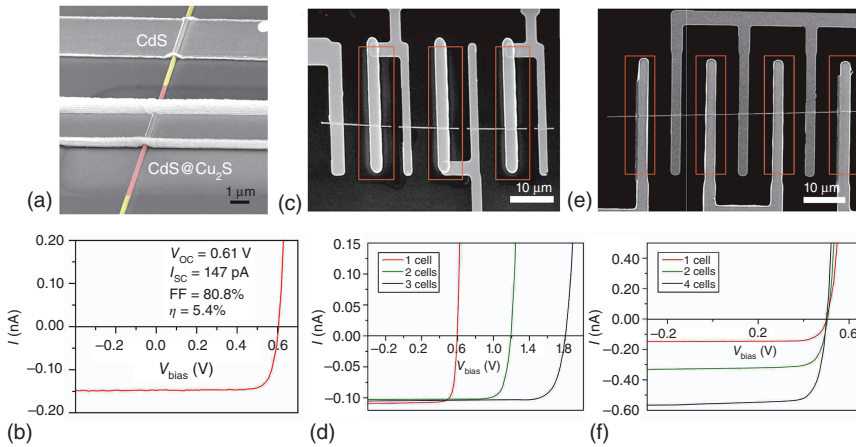


**Figure 1.7** (a) SEM picture of a PV unit with yellow and brown artificial dyes highlighting CdS and Cu<sub>2</sub>S, accordingly; (b)  $I$ - $V$  property of a fundamental nanowire exposed with (AM1.5G); (c) SEM picture of triple PV units in a sequence of a separate nanowire, showing the brown shapes indicating the core-shell areas; (d) the  $I$ - $V$  properties of the parallel devices within one sunlight irradiation (AM1.5G) demonstrate that the voltages add and the current remains unchanged; (e) SEM view shows four PV units off the single nanowire simultaneously, with brown boxes indicating the core-shell areas; and (f) during irradiation (AM1.5G), the  $I$ - $V$  property of the four perpendicular devices shows that the currents accumulate and the voltage remains constant. Source: Zhang et al. [102], MDPI, CC BY 4.0.

a linked p- and n-type NW technique. Additional NW processes have now been connected to the InP NWs electrode, such as p-Si/n-GaN, p-GaN/n-GaN, p-Si/n-CdS, and p-Si/n-CdSe [124, 125]. Ye et al. produced short-chain organic linker attached CsPbBr<sub>3</sub> NCs at room temperature in an ambient atmosphere [126]. They eventually succeeded in fabricating CsPbBr<sub>3</sub> NCs-based LED with a brightness of 5033 Cd/m<sup>-2</sup>, an external quantum efficiency (EQE) of 5.4%, and excellent thermal resilience [126]. Yassitepe and coworkers developed an alkaline production approach for nanocrystalline QDs, which resulted in coatings with low chemical composition and improved durability. Additionally, inversion QD-based red, green, and blue LEDs with EQE of 0.05%, 0.325%, and 0.075, respectively, were developed [127]. Demchyshyn and coworkers developed a new method for stabilizing perovskite materials. They enclosed perovskite NCs in an anodic aluminum oxide (AAO) thin film that served as an encapsulation scaffold, and the newly generated perovskite NCs' luminescence stability increased considerably. The photoluminescence quantum yield (PLQY) of these perovskite NCs was up to 90%, but only 0.03% EQE was attained, indicating that additional optimization of this design was required [128]. Duan et al. demonstrated infrared illumination from CdS NWs by attaining a large charge injecting frequency along the width of a CdS cavity that used a hybridized structure. The device's reduced temperature testing demonstrated a tendency for numerous extraction methods. The bandgap of the main emission line at 493 is 0.8 nm, which can be compared to the sensor resolution [129]. Tan and Friend et al. used perovskites to exhibit high electroluminescence. The color of the emission may

be altered by adjusting the perovskite layer's constitution. The wavelength of light emitted by  $\text{MAPbI}_3$  is 780 nm. The use of  $\text{Br}^-$  instead of  $\text{I}^-$  induces the emissive band to change to red and green hues. A sandwich arrangement was used to limit charge recombination inside the emissive layer, and quantum well structures give a high EL EQE of 0.8% [130].

Organic LED (OLED), inorganic quantum dots (QLEDs), and metal halide perovskites (PeLED)-based LED are leading in a new era of solid-state lighting where light can be modified as required [131]. OLEDs have offered up a range of unique options with exceptional flexibility over color, high contrast, and also reduced production procedures, while OLEDs also demonstrate an increasing position in the visual sectors [132, 133]. The adoption of defined techniques by the LED community to evaluate the performance of innovative materials and designs has resulted in various LED advancements and the self-sufficiency that this area requires to develop [134, 135]. LEDs, which are focused on a variety of transmitters including 3D, 2D, 1D, and 0D or double perovskites, have attracted a lot of interest in the illumination or display sectors. However, owing to a range of unique occurrences in these advanced technologies, which includes temporary impacts, these experimental results are often not explained in a cohesive and coherent method [131, 135, 136].

## 1.4 Conclusions

This book chapter explains the current achievements in fabrication, characterizations, and device implementation of 1D nanostructures. Either of the bottom-up and top-down techniques can be used to create 1D hybrid nanomaterials. The narrow shape and huge surface area of these nanomaterials allow them to be used in gas sensors and optoelectronic devices. However, despite the large amount of investigation being conducted in the field of 1D nanostructures, there seems to be a long way to go before they can be commercialized due to the challenges of scaling up manufacturing and maintaining characteristics throughout mass production.

## Acknowledgment

The authors are grateful to Department of Chemistry, Doon University, Uttarakhand, for providing the facilities for the successful completion of the reported work.

## References

- 1 Liu, X. and Li, Y. (2009). One-dimensional hybrid nanostructures with light-controlled properties. *Dalton Trans.* 33: 6447–6457.
- 2 Murray, C.B., Norris, D.J., and Bawendi, M.G. (1993). Synthesis and characterization of nearly monodisperse CdE (sulfur, selenium, tellurium) semiconductor nanocrystallites. *J. Am. Chem. Soc.* 115 (19): 8706–8715.

- 3 Fu, N., Li, Z., Myalitsin, A. et al. (2010). One-dimensional heterostructures of single walled carbon nanotubes and CdSe nanowires. *Small* 6 (3): 376–380.
- 4 Cui, Y. and Lieber, C.M. (2001). Functional nanoscale electronic devices assembled using silicon nanowire building blocks. *Science* 291 (5505): 851–853.
- 5 Peng, X., Chen, J., Misewich, J.A., and Wong, S.S. (2009). Carbon nanotube–nanocrystal heterostructures. *Chem. Soc. Rev.* 38 (4): 1076–1098.
- 6 Tan, C., Chen, J., Wu, X.J., and Zhang, H. (2018). Epitaxial growth of hybrid nanostructures. *Nat. Rev. Mater.* 3 (2): 17089.
- 7 Huang, X., Tan, C., Yin, Z., and Zhang, H. (2014). 25th anniversary article: hybrid nanostructures based on two dimensional nanomaterials. *Adv. Mater.* 26 (14): 2185–2204.
- 8 Tan, C. and Zhang, H. (2015). Two-dimensional transition metal dichalcogenide nanosheet-based composites. *Chem. Soc. Rev.* 44 (9): 2713–2731.
- 9 Fateixa, S., Nogueira, H.I.S., and Trindade, T. (2015). Hybrid nanostructures for SERS: materials development and chemical detection. *Phys. Chem. Chem. Phys.* 17 (33): 21046–21071.
- 10 Reddy, K.R., Hassan, M., and Gomes, V.G. (2015). Hybrid nanostructures based on titanium dioxide for enhanced photo catalysis. *Appl. Catal., A* 489: 1–16.
- 11 Du, N., Zhang, H., and Yang, D. (2012). One-dimensional hybrid nanostructures: synthesis via layer-by-layer assembly and applications. *Nanoscale* 4 (18): 5517–5526.
- 12 Wang, X., Song, J., Li, P. et al. (2005). Growth of uniformly aligned ZnO nanowire heterojunction arrays on GaN, AlN, and Al<sub>0.5</sub>Ga<sub>0.5</sub>N substrates. *J. Am. Chem. Soc.* 127 (21): 7920–7923.
- 13 Kovtyukhova, N.I., Kelley, B.K., and Mallouk, T.E. (2004). Coaxially gated in-wire thin-film transistors made by template assembly. *J. Am. Chem. Soc.* 126 (40): 12738–12739.
- 14 Vila-Fungueirino, J.M., Bachelet, R., Saint-Girons, G. et al. (2015). Integration of functional complex oxide nanomaterials on silicon. *Front. Phys.* 3: 38.
- 15 Peng, L., Zhang, Z., Wang, S., and Liang, X. (2012). A doping-free approach to carbon nanotube electronics and optoelectronics. *AIP Adv.* 2 (4): 041403.
- 16 Fu, Y., Zhu, H., Chen, J. et al. (2019). Metal halide perovskite nanostructures for optoelectronic applications and the study of physical properties. *Nat. Rev. Mater.* 4 (3): 169–188.
- 17 Zhao, Y.S., Fu, H., Peng, A. et al. (2010). Construction and optoelectronic properties of organic one-dimensional nanostructures. *Acc. Chem. Res.* 43 (3): 409–418.
- 18 Razeghi, M., Haddadi, A., Hoang, A.M. et al. (2014). Antimonide-based type II superlattices: a superior candidate for the third generation of infrared imaging systems. *J. Electron. Mater.* 43 (8): 2802–2807.
- 19 Tan, C.L. and Mohseni, H. (2018). Emerging technologies for high performance infrared detectors. *Nanophotonics* 7 (1): 169–197.
- 20 Sotiropoulou, S., Sierra-Sastre, Y., Mark, S.S., and Batt, C.A. (2008). Biotemplated nanostructured materials. *Chem. Mater.* 20 (3): 821–834.

- 21 Arole, V.M. and Munde, S.V. (2014). Fabrication of nanomaterials by top-down and bottom-up approaches-an overview. *JAAST Mater. Sci.* 1 (2): 89–93.
- 22 Chen, Y., Chadderton, L.T., Gerald, J.F., and Williams, J.S. (1999). A solid-state process for formation of boron nitride nanotubes. *Appl. Phys. Lett.* 74 (20): 2960–2962.
- 23 Fernandez, A., Reddy, E.P., Rojas, T.C., and Sanchez-Lopez, J.C. (1999). Application of the gas phase condensation to the preparation of nanoparticles. *Vacuum* 52 (1-2): 83–88.
- 24 Chepkasov, I.V., Gafner, Y.Y., Gafner, S.L., and Bardahanov, S.P. (2016). Condensation of Cu nanoparticles from the gas phase. *Phys. Met. Metall.* 117 (10): 1003–1012.
- 25 Colson, P., Henrist, C., and Cloots, R. (2013). Nanosphere lithography: a powerful method for the controlled manufacturing of nanomaterial. *J. Nanomater.* 2013: 948510.
- 26 Manouras, T. and Argitis, P. (2020). High sensitivity resists for EUV lithography: a review of material design strategies and performance results. *Nanomaterials* 10 (8): 1593.
- 27 Dhawan, A., Du, Y., Batchelor, D. et al. (2011). Hybrid top-down and bottom-up fabrication approach for wafer-scale plasmonic nanoplatforms. *Small* 7 (6): 727–731.
- 28 Shen, G. and Chen, D. (2009). One-dimensional nanostructure and device of II-V group semiconductor. *Nanoscale Res. Lett.* 4 (8): 779–788.
- 29 Kumar, S., Bhushan, P., and Bhattacharya, S. (2018). Fabrication of nanostructures with bottom-up approach and their utility in diagnostics, therapeutics, and others. In: *Environmental* (ed. S. Bhattacharya, A.A. Kumar, N. Chanda, et al.), 167–198. Singapore: Chemical and Medical Sensors.
- 30 Ploog, K. (1980). Molecular beam epitaxy of III–V compounds. In: III–V Semiconductors. In: *Crystals (Growth, Properties, and Applications)* (ed. H.C. Freyhardt), 73–162. Berlin Heidelberg: Springer-Verlag.
- 31 Cho, A.Y. and Arthur, J. (1975). Molecular beam epitaxy. *Prog. Solid State Chem.* 10 (3): 157–191.
- 32 Rothmund, P.W.K. (2005). Design of DNA origami. ICCAD-2005. In: *IEEE/ACM International Conference on Computer Aided Design*, vol. 2005, 471–448. IEEE.
- 33 Whitesides, G.M., Mathias, J.P., and Seto, C.T. (1991). Molecular self-assembly and nanochemistry: a chemical strategy for the synthesis of nanostructures. *Science* 254 (5036): 1312–1319.
- 34 Chen, Y., Xu, P., Xu, T. et al. (2017). ZnO-nanowire size effect induced ultra-high sensing response to ppb-level H<sub>2</sub>S. *Sens. Actuators, B* 240: 264–272.
- 35 Sharma, B., Sharma, A., and Myung, J.H. (2021). Selective ppb-level NO<sub>2</sub> gas sensor based on SnO<sub>2</sub>-boron nitride nanotubes. *Sens. Actuators, B* 331: 129464.
- 36 Bhowmik, B., Dutta, K., and Bhattacharyya, P. (2019). An efficient room temperature ethanol sensor device based on p-n homojunction of TiO<sub>2</sub> nanostructures. *IEEE Trans. Electron Devices* 66 (2): 1063–1068.
- 37 Li, X., Wang, Y., Le, Y., and Gu, Z. (2012). Highly sensitive H<sub>2</sub>S sensor based on template-synthesized CuO nanowires. *RSC Adv.* 2 (6): 2302–2307.

- 38 Wang, J.X., Sun, X.W., Yang, Y., and Wu, C.M.L. (2009). N–P transition sensing behaviors of ZnO nanotubes exposed to NO<sub>2</sub> gas. *Nanotechnology* 20 (46): 465501.
- 39 Lupan, O., Postica, V., Wolf, N. et al. (2017). Localized synthesis of iron oxide nanowires and fabrication of high performance nanosensors based on a single Fe<sub>2</sub>O<sub>3</sub> nanowire. *Small Methods* 13 (16): 1602868.
- 40 Navale, S.T., Yang, Z.B., Liu, C. et al. (2018). Enhanced acetone sensing properties of titanium dioxide nanoparticles with a sub-ppm detection limit. *Sens. Actuators, B* 255: 1701–1710.
- 41 Yan, S., Li, Z., Li, H. et al. (2018). Ultra-sensitive room-temperature H<sub>2</sub>S sensor using Ag–In<sub>2</sub>O<sub>3</sub> nanorod composites. *J. Mater. Sci.* 53 (24): 16331–16344.
- 42 Andre, R.S., Mercante, L.A., Facure, M.H.M. et al. (2019). Enhanced and selective ammonia detection using In<sub>2</sub>O<sub>3</sub>/reduced graphene oxide hybrid nanofibers. *Appl. Surf. Sci.* 473: 133–140.
- 43 Wang, X., Li, Z., Shi, J., and Yu, Y. (2014). One-dimensional titanium dioxide nanomaterials: nanowires, nanorods, and nanobelts. *Chem. Rev.* 114 (19): 9346–9384.
- 44 Hench, L.L. and West, J.K. (1990). The sol-gel process. *Chem. Rev.* 90 (1): 33–72.
- 45 Choi, K.S. and Chang, S.P. (2018). Effect of structure morphologies on hydrogen gas sensing by ZnO nanotubes. *Mater. Lett.* 230 (1): 48–52.
- 46 Sen, R., Govindaraj, A., and Rao, C.N. (1997). Carbon nanotubes by the metallocene route. *Chem. Phys. Lett.* 267 (3-4): 276–280.
- 47 Soares, O.S.G.P., Rocha, R.P., Gonçalves, A.G. et al. (2015). Easy method to prepare N-doped carbon nanotubes by ball milling. *Carbon* 91: 114–121.
- 48 Popov, V.N. (2004). Carbon nanotubes: properties and applications. *Mater. Sci. Eng., R* 43: 61–102.
- 49 Singh, N., Buddharaju, K.D., Manhas, S.K. et al. (2008). Si, SiGe nanowire devices by top-down technology and their applications. *IEEE Trans. Electron Devices* 55 (11): 3107–3118.
- 50 Hobbs, R.G., Petkov, N., and Holmes, J.D. (2012). Semiconductor nanowire fabrication by bottom-up and top-down paradigms. *Chem. Mater.* 24 (11): 1975–1991.
- 51 Shakhiviel, D., Ahmad, M., Alenezi, M.R. et al. (2019). *1D Semiconducting Nanostructures for Flexible and Large-Area Electronics: Growth Mechanisms and Suitability*, Elements in Flexible and Large Area Electronics (ed. R. Dahiya and L. Occhipinti), 1–98. Cambridge University Press.
- 52 Wu, Y., Yan, H., Huang, M. et al. (2002). Inorganic semiconductor nanowires: rational growth, assembly and novel properties. *Chem. Eur. J.* 8 (6): 1260–1268.
- 53 Wagner, R.S. and Ooherty, C.J. (1968). Mechanism of branching and kinking during VLS crystal growth. *J. Electrochem. Soc.* 115 (1): 93.
- 54 He, R., Gao, D., Fan, R. et al. (2005). Si nanowire bridges in microtrenches: integration of growth into device fabrication. *Adv. Mater.* 17 (17): 2098–2102.
- 55 Panda, D. and Tseng, T.Y. (2013). One-dimensional ZnO nanostructures: fabrication, optoelectronic properties, and device applications. *J. Mater. Sci.* 48 (20): 6849–6877.

- 56 Pauzauskie, P.J. and Yang, P. (2006). Nanowire photonics. *Mater. Today* 9 (10): 36–45.
- 57 Huang, M.H., Mao, S., Feick, H. et al. (2001). Room-temperature ultraviolet nanowire nanolasers. *Science* 292 (5523): 1897–1899.
- 58 Wagner, R.S. and Ellis, W.C. (1964). Vapor-liquid-solid mechanism of single crystal growth. *Appl. Phys. Lett.* 4 (5): 89–90.
- 59 Ghassan, A.A., Mijan, N.A., and Taufiq-Yap, Y.H. (2019). Nanomaterials: an overview of nanorods synthesis and optimization. In: *Nanorods and Nanocomposites* (ed. M.S. Ghamsari and S. Dhara), 1–24. London: Intech Open.
- 60 Li, L.S. and Alivisatos, A.P. (2003). Origin and scaling of the permanent dipole moment in CdSe nanorods. *Phys. Rev. Lett.* 90 (9): 097402.
- 61 Liu, J., Tanaka, T., Sivula, K. et al. (2004). Employing end-functional polythiophene to control the morphology of nanocrystal-polymer composites in hybrid solar cells. *J. Am. Chem. Soc.* 126 (21): 6550–6551.
- 62 Mutiso, R.M., Sherrott, M.C., Rathmell, A.R. et al. (2013). Integrating simulations and experiments to predict sheet resistance and optical transmittance in nanowire films for transparent conductors. *ACS Nano* 7 (9): 7654–7663.
- 63 Rao, M.V., Amareshwari, K., Viditha, V. et al. (2013). Flame synthesis of carbon nanorods with/without catalyst. *Int. J. Innov. Appl. Stud.* 3 (1): 1–5.
- 64 Yuan, Z., Li, R., Meng, F. et al. (2019). Approaches to enhancing gas sensing properties: a review. *Sensors* 19 (7): 1495.
- 65 Oh, E., Choi, H.Y., Jung, S.H. et al. (2009). High-performance NO<sub>2</sub> gas sensor based on ZnO nanorod grown by ultrasonic irradiation. *Sens. Actuators, B* 141 (1): 239–243.
- 66 Fine, G.F., Cavanagh, L.M., Afonja, A., and Binions, R. (2010). Metal oxide semi-conductor gas sensors in environmental monitoring. *Sensors* 10 (6): 5469–5502.
- 67 Nikolic, M.V., Milovanovic, V., Vasiljevic, Z.Z., and Stamenkovic, Z. (2020). Semiconductor gas sensors: materials, technology, design and application. *Sensors* 20 (22): 6694.
- 68 Rosty, R., Kebbekus, B., and Zaitsev, V. (2005). The testing of a semiconductor-based adsorption modified photosensitive sensor for its response to a volatile organic compound, oxygen, humidity and temperature. *Sens. Actuators, B* 107 (1): 347–352.
- 69 Huang, B., Lei, C., Wei, C., and Zen, G. (2014). Chlorinated volatile organic compounds (Cl-VOCs) in environment-sources, potential human impacts, and current remediation technologies. *Environ. Int.* 71: 118–138.
- 70 Wen, X., Fang, Y., Pang, Q. et al. (2005). ZnO nanobelt arrays grown directly from and on Zinc substrates: Synthesis, characterization, and applications. *J. Phys. Chem. B.* 109 (32): 15303–15308.
- 71 Fang, X., Hu, L., Ye, C., and Zhang, L. (2010). One-dimensional inorganic semiconductor nanostructures: a new carrier for nanosensors. *Pure Appl. Chem.* 82 (11): 2185–2198.
- 72 Velasco, G. and Schnell, J.P. (1983). Gas sensors and their applications in the automotive industry. *J. Phys. E: Sci. Instrum.* 16 (10): 973–977.

- 73 Leelakumar, M. (2020). Design of Electronic Control for Diesel Engines. In: *Design and Development of Heavy Duty Diesel Engines* (ed. P.A. Laxminarayanan and A.A. Kumar), 795–830. Singapore.
- 74 Masikini, M., Chowdhury, M., and Nemraoui, O. (2020). Metal oxides: application in exhaled breath acetone chemiresistive sensors. *J. Electrochem. Soc.* 167 (3): 037537.
- 75 Eddy, D.S. and Sparks, D.R. (1998). Application of MEMS technology in automotive sensors and actuators. *Proc. IEEE* 86 (8): 1747–1755.
- 76 Sun, P., Bisschop, R., Niu, H., and Huang, X. (2020). A review of battery fires in electric vehicles. *Fire Technol.* 56 (4): 1361–1410.
- 77 Nunes, D., Pimentel, A., Gonçalves, A. et al. (2019). Metal oxide nanostructures for sensor applications. *Semicond. Sci. Technol.* 34 (4): 043001.
- 78 Pavelko, R.G., Vasiliev, A.A., Llobet, E. et al. (2009). Comparative study of nanocrystalline SnO<sub>2</sub> materials for gas sensor application: thermal stability and catalytic activity. *Sens. Actuators, B* 137 (2): 637–643.
- 79 Padvi, M.N., Moholkar, A.V., Prasad, S.R., and Prasad, N.R. (2021). A critical review on design and development of gas sensing materials. *Eng. Sci.* 15: 20–37.
- 80 Kumar, R., Jaiswal, M., Singh, O. et al. (2019). Selective and reversible sensing of low concentration of carbon monoxide gas using Nb-doped OMS-2 nanofibers at room temperature. *IEEE Sens. J.* 19 (17): 7201–7206.
- 81 Wang, Z., Zhu, L., Sun, S. et al. (2021). One dimensional nanomaterial in resistive gas sensor: from material design to application. *Chemosensors* 9 (8): 198–200.
- 82 Raza, M.H., Kaur, N., Comini, E., and Pinna, N. (2020). Toward optimized radial modulation of the space-charge region in one-dimensional SnO<sub>2</sub>-NiO core-shell nanowires for hydrogen sensing. *ACS Appl. Mater. Interfaces* 12 (4): 4594–4606.
- 83 Nikfarjam, A., Hosseini, S., and Salehifar, N. (2017). Fabrication of a highly sensitive single aligned TiO<sub>2</sub> and gold nanoparticle embedded TiO<sub>2</sub> nano-fiber gas sensor. *ACS Appl. Mater. Interfaces* 9 (18): 15662–15671.
- 84 Spetz, A.L., Unéus, L., Svenningstorp, H. et al. (2001). SiC based field effect gas sensors for industrial applications. *Phys. Stat. Sol.* 185 (1): 15–25.
- 85 Shimizu, Y., Matsunaga, N., Hyodo, T., and Egashira, M. (2001). Improvement of SO<sub>2</sub> sensing properties of WO<sub>3</sub> by noble metal loading. *Sens. Actuators, B* 77 (2): 35–40.
- 86 Sowmya, B., John, A., and Panda, P.K. (2021). A review on metal-oxide based p-n and n-n hetero structured nanomaterials for gas sensing applications. *Sens. Int.* 2 (3): 100085.
- 87 Tao, W.H. and Tsai, C.H. (2002). H<sub>2</sub>S sensing properties of noble metal doped WO<sub>3</sub> thin film sensor fabricated by micromachining. *Sens. Actuators, B* 81 (2-3): 237–247.
- 88 Kuswandi, B., Wicaksono, Y., Jayus, A.A. et al. (2011). Smart packaging: sensors for monitoring of food quality and safety. *Sens. Instrum. Food Qual. Saf.* 5 (3): 137–146.
- 89 Kim, N.H., Choi, S.J., Yang, D.J. et al. (2014). Highly sensitive and selective hydrogen sulfide and toluene sensors using Pd functionalized WO<sub>3</sub> nanofibers for potential diagnosis of halitosis and lung cancer. *Sens. Actuators, B* 193 (193): 574–581.

- 90 Ama, O., Sadiq, M., Johnson, M. et al. (2020). Novel 1D/2D KWO/Ti<sub>3</sub>C<sub>2</sub>T<sub>x</sub> nanocomposite-based acetone sensor for diabetes prevention and monitoring. *Chemosensors* 8 (4): 102.
- 91 Wang, X., Li, Y., Pionteck, J. et al. (2018). Flexible poly(styrene-butadiene-styrene)/carbon nanotube fiber based vapor sensors with high sensitivity, wide detection range and fast response. *Sens. Actuators, B* 256: 896–904.
- 92 Gong, H., Zhao, C., Niu, G. et al. (2020). Construction of 1D/2D  $\alpha$ -Fe<sub>2</sub>O<sub>3</sub>/SnO<sub>2</sub> hybrid nanoarrays for sub-ppm acetone detection. *Res. Sci. Partner J.* 2020: 2196063.
- 93 Moon, S.E., Choi, N.J., Lee, H.K. et al. (2013). Semiconductor-type MEMS gas sensor for real-time environmental monitoring applications. *ETRI J.* 35 (4): 617–624.
- 94 Tomchenko, A.A., Harmer, G.P., Marquis, B.T., and Allen, J.W. (2003). Semiconducting metal oxide sensor array for the selective detection of combustion gases. *Sens. Actuators, B* 93 (1-3): 126–134.
- 95 Ibrahim, R.K., Hayyan, M., AlSaadi, M.A. et al. (2016). Environmental application of nanotechnology: air, soil, and water. *Environ. Sci. Pollut. Res.* 23 (14): 13754–13788.
- 96 Yamazoe, N. and Miura, N. (1994). Environmental gas sensing. *Sens. Actuators, B* 20 (2-3): 95–102.
- 97 Suh, J.M., Kwon, K.C., Lee, T.H. et al. (2021). Edge-exposed WS<sub>2</sub> on 1D nanostructures for highly selective NO<sub>2</sub> sensor at room temperature. *Sens. Actuators, B* 333: 129566.
- 98 Dai, W., Yu, J., Luo, S. et al. (2020). WS<sub>2</sub> quantum dots seeding in Bi<sub>2</sub>S<sub>3</sub> nanotubes: a novel Vis-NIR light sensitive photocatalyst with low-resistance junction interface for CO<sub>2</sub> reduction. *Chem. Eng. J.* 389: 123430.
- 99 Lim, K., Jo, Y.M., Yoon, J.W. et al. (2021). A transparent nanopatterned chemiresistor: visible light plasmonics sensor for trace level NO<sub>2</sub> detection at room temperature. *Small* 17 (20): 2100438.
- 100 Cui, S., Pu, H., Lu, G. et al. (2012). Fast and selective room-temperature ammonia sensors using silver nanocrystal-functionalized carbon nanotubes. *ACS Appl. Mater. Interfaces* 4 (9): 4898–4904.
- 101 Pescaglioni, A. and Iacopino, D. (2015). Metal nanoparticle–semiconductor nanowire hybrid nanostructures for plasmon-enhanced optoelectronics and sensing. *J. Mater. Chem. C* 3 (45): 11785–11800.
- 102 Zhang, X., Wu, D., and Geng, H. (2017). Heterojunctions based on II-VI compound semiconductor one dimensional nanostructures and their optoelectronic applications. *Crystals* 7 (10): 307.
- 103 Jeon, N.J., Noh, J.H., Yang, W.S. et al. (2015). Compositional engineering of perovskite materials for high-performance solar cells. *Nature* 517 (7535): 476–480.
- 104 Liu, J., Yang, Z., Ye, B. et al. (2019). A review of stability-enhanced luminescent materials: fabrication and optoelectronic applications. *J. Mater. Chem. C* 7 (17): 4934–4955.

- 105 Hyun, J.K. and Lauhon, L.J. (2011). Spatially resolved plasmonically enhanced photocurrent from Au nanoparticles on a Si nanowire. *Nanoletters* 11 (7): 2731–2734.
- 106 Grinblat, G., Rahmani, M., Cortés, E. et al. (2014). High efficiency second harmonic generation from a single hybrid ZnO nanowire/Au plasmonic nano-oligomer. *Nano Lett.* 14 (11): 6660–6665.
- 107 Knight, M.W., Sobhani, H., Nordlander, P., and Halas, N.J. (2011). Photodetection with active optical antennas. *Science* 332 (6030): 702–704.
- 108 Kawawaki, T., Wang, H., Kubo, T. et al. (2015). Efficiency enhancement of PbS quantum dot/ZnO nanowire bulk-heterojunction solar cells by plasmonic silver nanocubes. *ACS Nano* 9 (4): 4165–4172.
- 109 Chen, W., Hao, J., Hu, W. et al. (2017). Enhanced stability and tunable photoluminescence in perovskite CsPbX<sub>3</sub>/ZnS quantum dot heterostructure. *Small* 13 (21): 1604085.
- 110 Jie, J., Zhang, W., Bello, I. et al. (2010). One-dimensional II–VI nanostructures: synthesis, properties and optoelectronic applications. *Nanotoday* 5 (4): 313–336.
- 111 Chen, Q., De Marco, N., Yang, Y.M. et al. (2015). Under the spotlight: the organic-inorganic hybrid halide perovskite for optoelectronic applications. *Nanotoday* 10 (3): 355–338.
- 112 Luo, L.B., Xie, W.J., Zou, Y.F. et al. (2015). Surface plasmon propelled high-performance CdSe nanoribbons photodetector. *Opt. Express* 23 (10): 12979–12988.
- 113 Dong, R., Fang, Y., Chae, J. et al. (2015). High-gain and low-driving-voltage photodetectors based on organolead triiodide perovskites. *Adv. Mater.* 27 (11): 1912–1918.
- 114 Wang, L., Chen, R., Ren, Z.F. et al. (2016). Plasmonic silver nanosphere enhanced ZnSe nanoribbon/Si heterojunction optoelectronic devices. *Nanotechnology* 27 (21): 215202.
- 115 Dou, L., Yang, Y.M., You, J. et al. (2014). Solution-processed hybrid perovskite photodetectors with high detectivity. *Nat. Commun.* 5 (1): 5404.
- 116 Afzaal, M. and Brien, P. (2006). Recent developments in II–VI and III–VI semiconductors and their applications in solar cells. *J. Mater. Chem.* 16 (17): 1597–1602.
- 117 Ferekides, C.S., Balasubramanian, U., Mamazza, R. et al. (2004). CdTe thin film solar cells: device and technology issues. *Sol. Energy* 77 (6): 823–830.
- 118 Bamola, P., Rana, S., Singh, B. et al. (2021). Nanostructured oxide based ceramic materials for light and mechanical energy harvesting applications. In: *Advanced Ceramics for Energy and Environmental Applications*, vol. 11 (ed. A. Kumar), 116–135. Boca Raton.
- 119 Wu, D., Jiang, Y., Li, S. et al. (2011). Construction of highquality CdS: Ga nanoribbon/silicon heterojunctions and their nano-optoelectronic applications. *Nanotechnology* 22: 405201.
- 120 Zhang, X., Zhang, X., Wang, L. et al. (2013). ZnSe nanowire/Si p heterojunctions: device construction and optoelectronic applications. *Nanotechnology* 24 (39): 395201.

- 121 Wong, A.B., Brittman, S., Yu, Y. et al. (2015). Core-shell CdS-Cu<sub>2</sub>S nanorod array solar cells. *Nano Lett.* 15 (6): 4096–4101.
- 122 Tvingstedt, K., Malinkiewicz, O., Baumann, A. et al. (2014). Radiative efficiency of lead iodide based perovskite solar cells. *Sci. Rep.* 4: 6071.
- 123 Duan, X., Huang, Y., Cui, Y. et al. (2001). Indium phosphide nanowires as building blocks for nanoscale electronic and optoelectronic devices. *Nature* 409 (6816): 66–69.
- 124 Huang, Y., Duan, X., and Lieber, C.M. (2005). Nanowires for integrated multicolor nanophotonics. *Small* 1 (1): 142–147.
- 125 Li, Y., Qian, F., Xiang, J., and Lieber, M. (2006). Nanowire electronic and optoelectronic devices. *Mater. Today* 9 (10): 18–27.
- 126 Ye, F., Zhang, H., Li, W. et al. (2019). Ligand-exchange of low-temperature synthesized CsPbBr<sub>3</sub> perovskite toward high efficiency light emitting diodes. *Small Methods* 3 (3): 1800489.
- 127 Yassitepe, E.Y., Yang, Z., Voznyy, O. et al. (2016). Amine-free synthesis of cesium lead halide perovskite quantum dots for efficient light emitting diodes. *Adv. Funct. Mater.* 26 (47): 8757–8763.
- 128 Demchysyan, S., Roemer, J.M., Groib, H. et al. (2017). Confining metal-halide perovskites in nanoporous thin films. *Sci. Adv.* 3 (8): 1700738.
- 129 Duan, X., Huang, Y., Agarwal, R., and Lieber, C.M. (2003). Single-nanowire electrically driven lasers. *Nature* 421: 241–245.
- 130 Tan, Z.K., Moghaddam, R.S., Lai, M.L. et al. (2014). Bright light-emitting diodes based on organometal halide perovskite. *Nat. Nanotechnol.* 9 (9): 687–692.
- 131 Anaya, M., Rand, B.P., Holmes, R.J. et al. (2019). Best practices for measuring emerging light-emitting diode technologies. *Nat. Photonics* 13 (12): 818–821.
- 132 Greenham, N.C., Friend, R.H., and Bradley, D.D.C. (1994). Angular dependence of the emission from a conjugated polymer light-emitting diode: implications for efficiency calculations. *Adv. Mater.* 6 (6): 491–494.
- 133 Chen, H.W., Lee, J.H., Lin, B.Y. et al. (2018). Liquid crystal display and organic light-emitting diode display: present status and future perspectives. *Light Sci. Appl.* 7 (3): 17168.
- 134 Long, X., He, J., Zhou, J. et al. (2015). A review on light-emitting diode based automotive headlamps. *Renewable Sustainable Energy Rev.* 41: 29–41.
- 135 Zhao, B., Bai, S., Kim, V. et al. (2018). High-efficiency perovskite-polymer bulk heterostructure light-emitting diodes. *Nat. Photonics* 12 (12): 783–789.
- 136 Lin, K., Xing, J., Quan, L.N. et al. (2018). Perovskite light-emitting diodes with external quantum efficiency exceeding 20 per cent. *Nature* 562 (7726): 245–248.